

Mo-Doped BiVO₄ as a Fast Electrode Reaction Kinetics Catalyst in Na—O₂ Batteries

Minglu Li⁺^[a], Jiazhi Wang⁺^[c], Wei He,^[a] Xiong Zhang,^[b, d] Huijuan Zhang,^[a, b] Jinling Ma,*^[a] and Yu Wang^[a, b]

The highly insulated solid discharge products in sodium-oxygen (Na—O₂) batteries induce large polarization and thus heavily threaten their cycle life. Controlment of discharge products taking efficient catalyst is a best way to solve this problem. Here, Mo-doped BiVO₄ as the catalyst produces large amounts of carrier, thus boosting the battery reaction and reducing the overpotential under the light assistance. Compared with the BiVO₄ without Mo doping, the doped one has a lower recombination of photogenerated carriers, thus benefiting a large polarization suppression and Na—O₂ batteries running for over 270 cycles under 3.65 V as well as a fine rate performance.

Besides, Mo doping reduces the size of BiVO₄, beneficial for the carrier transportation and more reactions due to the large specific surface area. Experiment combined with theoretical calculation shows that Mo doping is advantageous to enhancing catalytic activity of BiVO₄ due to a lower work function for easier electron extraction, thus enhancing Na₂O₂ decomposition capability. This work undoubtedly inspires photocatalysts' use for solving the insulated solid discharge products decomposition in metal-O₂ batteries and provides a guide for other photocatalysts possibilities.

1. Introduction

With energy crisis and climate warm, the development and utilization of clean energy has become man's consensus.^[1] However, clean energy utilization highly depends on energy storage and conversion device. At present, electrochemical energy storage and conversion device, such as batteries have become the power core in e-vehicle and mobility. Under the limitation of the theoretical energy density of Li-ion batteries, mile anxiety and the increasing cost of raw material in Li-ion batteries push man to develop other candidates with much higher energy density.^[2–6] Undoubtedly, Na batteries, such as Na-ion and Na-oxygen batteries become the best candidate because of the low cost and similar properties to Li. The energy density of Na-oxygen batteries has several times higher than that of Na-ion one, but its research is later. Na—O₂ batteries also face many similar problems to other batteries, such as the instability of anode, electrolyte as well as low catalytic activity of cathode.

Among them, a highly efficient cathode is very important to solving the anode and electrolyte problems. On the cathode side, the insulated solid products such as Na₂O₂ formed after discharge would cover on the cathode and prevent further discharging. Subsequently, the discharge products need high charging potential to decompose, thus causing the decomposition of electrolyte accompanying with many insulated side products, which continues to deteriorate battery and shorten its cycle life.^[4] Therefore, designing a catalyst/cathode to decompose the discharge products with a low charge potential is very important and urgent for Na—O₂ battery development.^[8,9]

At present, many works are focused on the solid electrochemical catalysts, such as precious metals and transition metal oxides.^[10–12] However, precious metal catalyst has very high cost. Despite of its high catalytic activity, its large-scale application is impossible. Transition metal oxides have a high theoretical catalytic activity, but are limited by intrinsic insulated properties and continuous accumulated undecomposed products covering, resulting their final deactivation. Soluble redox mediators can greatly reduce charging overpotential, but their use may bring about anode degradation, namely shuttle effects and the catalytic activity continuously decreases with the consumption of redox mediator by anode.^[13] But soluble redox mediator indeed gives an inspiration, namely indirectly producing a more active mediator to react with discharge products. Photocatalyst under light irritation can produce more active electrons and holes, thus instantly improving the conductivity of the electrode, which can accelerate the electron transfer for faster reactions. Theoretically, fast reactions in Na—O₂ batteries can benefit one-electron reaction for producing NaO₂ discharge products with a low potential to decompose.^[14] Photocatalyst speeding up battery reactions has been verified by our previous study using BiVO₄.^[15]

[a] M. Li,⁺ W. He, H. Zhang, J. Ma, Y. Wang

State Key Laboratory of Power Transmission Equipment Technology, School of Electrical Engineering, Chongqing University, 174 Shazheng Street, Shapingba District, Chongqing City, 400044, P.R. China
E-mail: majinling@ciac.ac.cn

[b] X. Zhang, H. Zhang, Y. Wang

School of Chemistry and Chemical Engineering, Chongqing University, 174 Shazheng Street, Shapingba District, Chongqing City, 400044, P.R. China

[c] J. Wang⁺

National Research Center for Physical Sciences at the Microscale University of Science and Technology of China Hefei, Anhui, 230026, P.R. China

[d] X. Zhang

Qingan Energy Storage Technology Co., Ltd, Chongqing City, 402247, P.R. China

[+] These authors contributed equally to this work.

 Supporting information for this article is available on the WWW under <https://doi.org/10.1002/batt.202400066>

It is reported that approximately 60%–80% of the charge carriers generated by pure BiVO_4 under illumination will recombine before reaching the material surface, resulting in low light quantum yield. The low light quantum yield is related to the slow electron mobility of BiVO_4 , thus greatly increasing the possibility of recombination. In order to obtain higher charge carrier concentration. Two methods are often used: one is to reduce the size of BiVO_4 , the other is doping heteroatoms. The former is due to the shorted distance of charge carrier reached to surface.^[16] The latter can change the crystal symmetry of BiVO_4 and introduce some polarons, making it more difficult for recombining generated electrons with holes. In most researches, Mo doping is reported to be the most efficient way to improve the photocatalytic performance of BiVO_4 because Mo^{6+} can be doped into BiVO_4 to replace the position of some V^{5+} , which would change the crystal symmetry of BiVO_4 .^[17,18] Meanwhile, as a hexavalent ion, Mo^{6+} can serve as shallow donors to provide additional free electrons and further increase carrier concentration, thereby improving material conductivity.^[19]

Here, we studied the influence of Mo doping contents in BiVO_4 on the performance of $\text{Na}-\text{O}_2$ batteries. Interestingly, compared with pure BiVO_4 , Mo doping not only reduces the size of BiVO_4 , exposing more surface areas, but also has a lower recombination of photogenerated carriers. When the doping is 7%, BiVO_4 realized an optimal light quantum yield as well as recombination of charge carrier. This improves $\text{Na}-\text{O}_2$ batteries reaction kinetics, thus advantageous to the one-electron reaction, which helps $\text{Na}-\text{O}_2$ batteries run for over 270 cycles under 3.65 V as well as a fine rate capability. Theoretical calculation shows the Mo-doped BiVO_4 a finer light excitation as well as a stronger accepting electron from Na_2O_2 beneficial for facilely decomposing Na_2O_2 .

2. Results

BiVO_4 prepared under different doping concentrations is named MBV-n, where MBV and n represent the Mo-doped BiVO_4 and Mo molar percentage occupied in V position relative to Bi, respectively. For example, MBV-7 is the abbreviation of $\text{BiMo}_{0.07}\text{V}_{0.93}\text{O}_4$.

X-ray diffraction (XRD) is conducted to determine the crystalline phase of BiVO_4 . From Figure 1a, it can be seen that the MBV-0 exhibits a distinct monoclinic BiVO_4 (JCPDS 14-0688) characteristic peak. Meanwhile, the diffraction peaks of different contents Mo-doped-samples also correspond to monoclinic BiVO_4 , proving that the doping of Mo caused no phase change of BiVO_4 . In MBV-10, except for the peaks of BiVO_4 , there appeared MoO_3 peaks (JCPDS 21-0569). It is reported that supersaturated Mo ion tends to form MoO_3 particles near the surface of BiVO_4 , which would act as the recombination sites for photo generated carriers, resulting in a significant decrease in carrier concentration.^[20] It is worth noting that due to the larger size of doped Mo^{6+} compared to V^{5+} , doping can cause lattice expansion.^[19] This lattice expansion is verified by the partial enlarged image of XRD patterns (Figure 1b), which indicated that compared to MBV-0, the (121) peaks of Mo-doped BiVO_4 displayed a slight shift to lower angle, indicating that Mo^{6+} has successfully doped into BiVO_4 .

Figure 1c shows the UV-vis diffuse reflectance spectra of MBV-0, MBV-5, MBV-7 and MBV-10. All four samples show same absorption peak positions, which is consistent with the previously reported monoclinic BiVO_4 absorption peak.^[21,22] In addition, the UV-vis diffuse reflectance spectra of the four samples almost completely overlap in the wavelength range of 550–800 nm. As the doping concentration increases, the absorption intensity of the sample significantly increases in the wavelength range of 250–470 nm, and reaches a maximum value at a doping concentration of 7%. The spectra of MBV-10 are almost consistent with MBV-7 thereafter. When

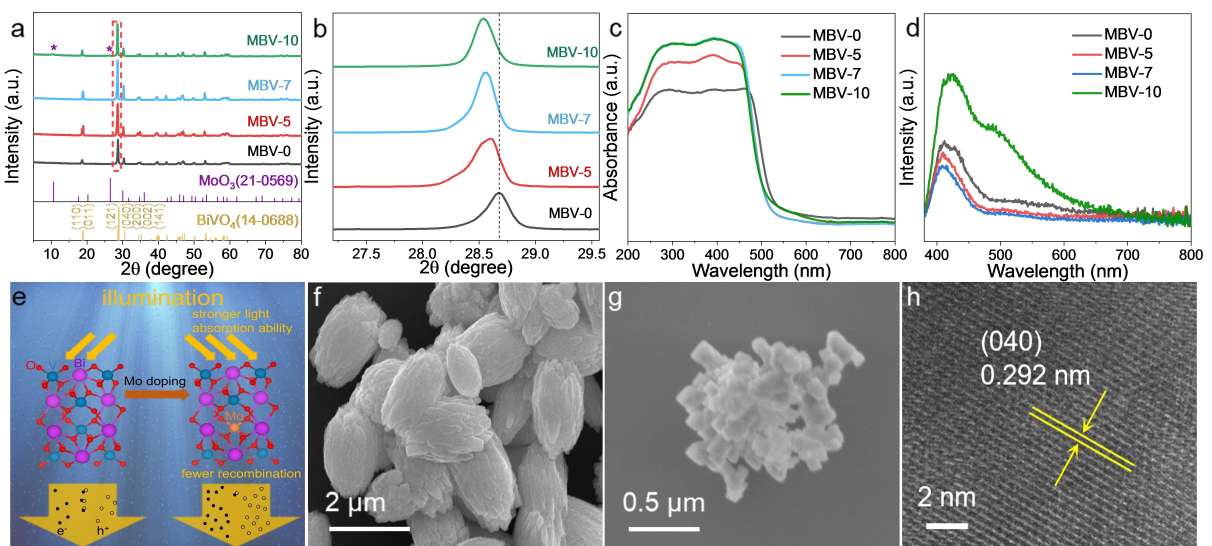


Figure 1. a) XRD patterns, and b) its partial enlarged image, c) UV-vis diffuse reflectance spectra, d) PL spectra for MBV; e) schematic diagram of Mo doping improving BiVO_4 catalytic performance; SEM images for f) MBV-0, and g) MBV-7; h) HRTEM images for MBV-7.

photo generated electrons and holes recombine, energy is released. The released energy can be detected by the Photoluminescence (PL) spectra. By comparing the peak intensity of the PL spectra of different materials, the recombination capability of charge carrier or the separation efficiency of photogenerated electrons and holes can be determined. In our case, PL spectra of four samples were obtained. As shown in Figure 1d, all the four samples exhibit emission intensities in the range of 375–550 nm. Among them, the emission intensity for MBV-7 is the weakest, and it is well known that the lower PL intensity indicates higher separation efficiency, which may lead to higher photocatalytic activity as schemed in Figure 1e.^[23] It is worth noting that the emission intensity of MBV-10 is much higher than those of the other three samples. According to the results shown in Figure 1a, MoO₃ particles in MBV-10 may serve as composite sites for photogenerated electrons and holes and induce severe recombination accompanying with a significant decrease in photo generated carrier concentration, which possibly ultimately reduces the photocatalytic activity of the material.^[20] Based on MBV-7 the highest light absorption intensity as well as its highest separation efficiency of charge carrier, it was selected as the optimal doped photocatalyst for comparative experiments with the original MBV-0 to further investigate its performance and catalytic mechanism.

SEM image of MBV-0 (Figure 1f) shows elliptical in shape, with a relatively smooth surface and a particle size of approximately 2 μm. The MBV-7 exhibits extremely irregular shape and a smaller size (<200 nm) (Figure 1g), which possibly is caused by Mo salt introduction to affect the growth pattern of crystals as ever reported.^[24] This also indicates MBV-7 a higher specific surface area, as evidenced by the BET results shown in the Figure S1. The specific surface area of MBV-7 is

4.7085 m² g⁻¹, much higher than that of MBV-0 (1.4163 m² g⁻¹). The smaller size makes it easier for the photo generated charge carriers of MBV-7 to reach its surface and exert their effects. Besides, a larger specific surface area can provide more active sites. The high-resolution TEM images for MBV-7 (Figure 1h) and MBV-0 (Figure S2) both show distinct lattice spacing of 0.292 nm corresponding to (040) crystal planes. The evident lattice stripes indicate that the crystal surface is stable.

To verify the success of Mo doping, the elemental distribution is analyzed by TEM element mapping and distribution. As shown in Figure 2a and b, both of the MBV-0 and MBV-7 show the uniform distribution of the basic Bi, V, and O elements. For MBV-7, Mo element distribution is the same as that of basic elements without any element clustering, quite consistent with the High-Angle Annular Dark-Field (HAADF) image of MBV-7. This shows Mo uniform distribution and successful doping in MBV-7. The inductively coupled plasma (ICP) test show 1.97% (mass ratio) Mo in MBV-7 (Table S1), almost in line with the theoretical calculated result (2.055%), proving that the doping is successful.

The valence and composition of MBV-0 and MBV-7 were studied using X-ray Photoelectron Spectroscopy (XPS) (Figure S3). The signals of Bi 4f_{7/2} and Bi 4f_{5/2} cause the binding energy of Bi 4f XPS spectrum (Figure 2c) to concentrate around 164.5 and 159.2 eV respectively. The binding energy of V 2p XPS caused by V⁵⁺ is located at 516.8 and 524.3 eV respectively (Figure 2d). The XPS spectra of Bi 4f and V 2p in MBV-0 and MBV-7 are almost consistent. The O 1s spectrum of MBV-0 (Figure 2e) was deconvoluted into two peaks (529.9 and 531.7 eV), indicating the presence of at least two types of O species. According to the ever report, the peak at 531.7 eV is attributed to the surface adsorbed O, while the signal at 529.9 eV is a characteristic of lattice O in BiVO₄.^[25,26] The O 1s spectrum of MBV-7 (Figure 2e) is deconvoluted into two peaks

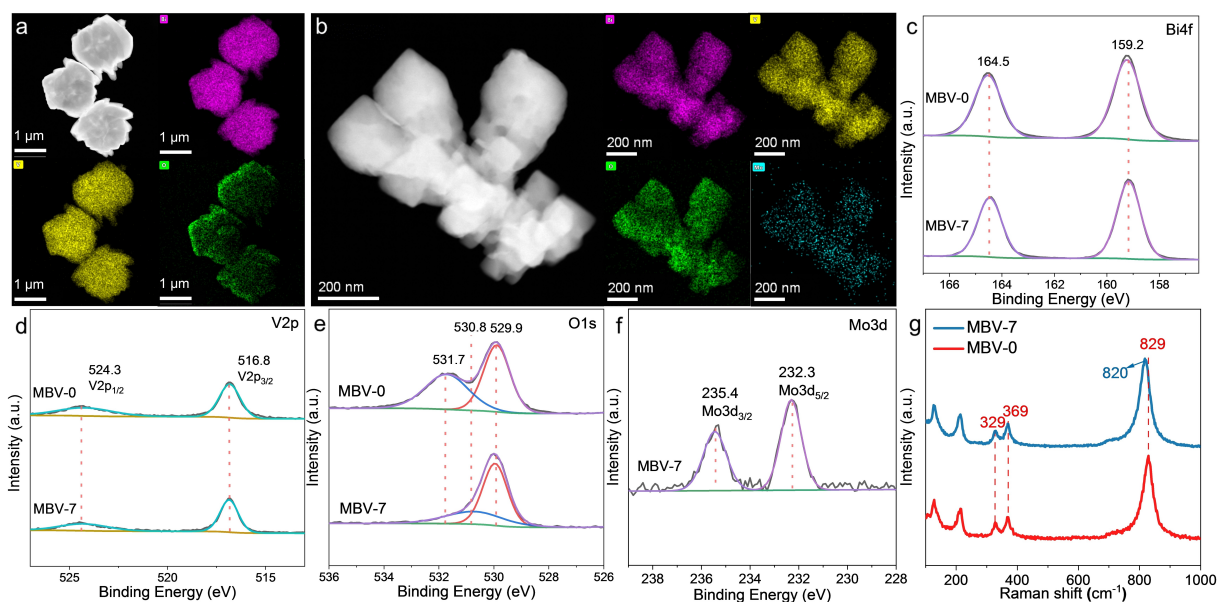


Figure 2. HAADF images and TEM element mapping of the a) MBV-0, and b) MBV-7; XPS spectra of c) Bi 4f, d) V 2p, e) O 1s and f) Mo 3d; and g) Raman spectra of BiVO₄.

at 529.9 and 530.8 eV, and the peak at 531.7 eV disappears, indicating a lower oxygen vacancy concentration on the surface of BiVO_4 after Mo doping. The binding energy (Figure 2f) of Mo $3\text{d}_{5/2}$ and Mo $3\text{d}_{3/2}$ are 232.3 and 235.4 eV respectively, indicating that the dopant Mo in the form of Mo^{6+} ion is bound to the lattice site of BiVO_4 as ever reported.

The Raman spectra in Figure 2g show the symmetric and asymmetric bending modes of V–O in the VO_4 tetrahedron centered at 369 and 329 cm^{-1} , respectively underwent no shift, but the stretching mode at 829 cm^{-1} in MBV-0 corresponding to symmetric V–O appeared a slight red shift for MBV-7 (820 cm^{-1}), which possibly was attributed to the displacement of V^{5+} by Mo^{6+} in the BiVO_4 lattice.^[27,28]

Electrochemical impedance spectroscopy (EIS) measurements were performed in a 2.5 mmol/L potassium ferrocyanide solution using ITO loaded with BiVO_4 as the working electrode, Pt electrode as the counter electrode, and Ag/AgCl as the reference electrode. As shown in Figure 3a, the Nyquist plot of MBV-7 displays two semicircular arc features with two different charge transfer mechanisms. The high-frequency semicircular arc corresponds to the bulk properties or impedance of grains, while the intermediate frequency semicircular arc represents the impedance of grain boundaries.^[29] However, in the MBV-0, grain impedance is too high, so its Nyquist plot exhibits a large

approximate semicircular arc in the high and medium frequency regions (Table S2). In addition, the MBV-7 has a lower interface charge transfer resistance according to the smaller semicircle arc at high frequencies than MBV-0, indicating the MBV-7 a higher photogenerated carrier concentration under illumination and lower recombination rate of carriers, which corresponded to the results of PL.^[14,30] All these are attributed to the faster electron transfer rate of MBV-7.

To elucidate the relationship between the photocurrent response of BiVO_4 and the performance of $\text{Na}-\text{O}_2$ batteries, two BiVO_4 samples mixed with conductive CNTs were used as cathodes and tested in $\text{Na}-\text{O}_2$ batteries. The analysis of battery performance test results, unless otherwise specified, is obtained under the illumination of a light source. The analysis of battery performance testing results would use the catalyst name to refer to the battery. Figure 3b shows the CV curves of $\text{Na}-\text{O}_2$ batteries using MBV-0 and MBV-7 as catalysts. Generally speaking, the smaller the voltage difference between the oxidation and reduction peaks from the CV curve, the smaller the polarization and the possibly more stable the battery performance. Compared with MBV-0 (0.283 V), the bimodal voltage difference of MBV-7 (0.282 V) is slightly lower, indicating a smaller polarization. The oxidation and reduction peaks in the two batteries displayed a quasi-symmetry feature, revealing

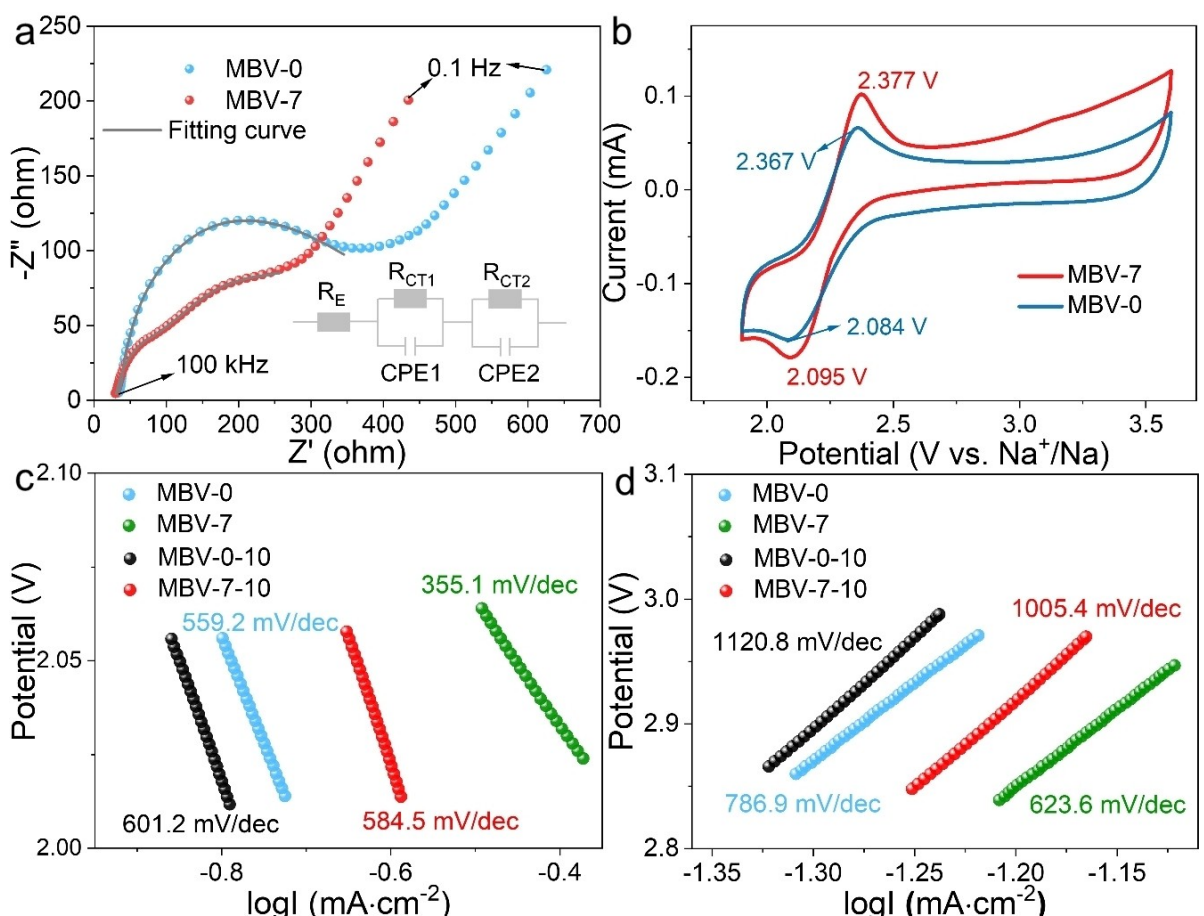


Figure 3. a) EIS under illumination, b) CV curves, c) the Tafel slope for ORR and OER after 10 cycles discharge/charge, d) the Tafel slope for OER and OER after 10 cycles discharge/charge for MBV-0 and MBV-7 in $\text{Na}-\text{O}_2$ batteries.

quasi-reversible battery reactions. The higher intensity the peak, the greater the current, indicating more reaction sites and reactions in the material. Obviously, the oxygen reduction reaction (ORR) part of CV curve shows the MBV-7 a higher reduction current density, which proves more reduction reactions on it. Meanwhile, in the oxygen evolution reaction (OER) part of the CV curve, MBV-7 also exhibits a higher OER current density, indicating a more favorable OER reaction on the MBV-7 cathode.

The Tafel slope derived from the LSV curve (Figure S4) can be used to describe the kinetics of electrochemical reactions, with a smaller slope indicating a higher reaction rate. Figure 3c shows that the Tafel slope value of MBV-7 for ORR ($355.1 \text{ mV dec}^{-1}$) was smaller than MBV-0 ($559.2 \text{ mV dec}^{-1}$), indicating the MBV-7 a more excellent ORR reaction kinetics. Due to the formation of solid electrolyte interface (SEI) and/or side products covering, the polarization of Na-O₂ batteries would increase and result in the current density decreasing (Figure S4c). After 10 cycles discharge/charge testing, the MBV-7 still has a higher reduction current density, demonstrating its improved catalytic performance. The Tafel slope value of MBV-7 ($584.5 \text{ mV dec}^{-1}$) for ORR running after 10 battery discharge/charge cycles is still smaller than that of MBV-0 ($601.2 \text{ mV dec}^{-1}$) after the same cycles, once again proving the MBV-7 a more excellent ORR reaction kinetics. Similarly, Figure 3d shows that the Tafel slope value of MBV-7 ($623.6 \text{ mV dec}^{-1}$) for OER is smaller than that of MBV-0 ($786.9 \text{ mV dec}^{-1}$), indicating the MBV-7 faster OER kinetics. Moreover, in the OER part of the LSV curve (Figure S4d), the MBV-7 after 10 cycles also showed higher OER current density, indicating a more favorable OER reaction on the MBV-7 cathode. Meanwhile, the Tafel slope value of MBV-7 ($1005.4 \text{ mV dec}^{-1}$) for OER running after 10 cycles is smaller than that of MBV-0 ($1120.8 \text{ mV dec}^{-1}$), further proving the MBV-7 faster OER kinetics.

The EIS results of the pristine batteries are shown in Figure 4a. The semicircle in the EIS diagram is attributed to interface resistance and charge transfer resistance. Obviously, the impedance of MBV-7 is lower, indicating its possible fast charge transfer. Besides, after ruing 10 discharge/charge cycles, EIS results showed a lower impedance of Na-O₂ batteries with the MBV-7 catalyst than that with the MBV-0 (Figure 4b). The increase in impedance for the two sets of batteries compared to the initial could be attributed to the incomplete decomposition of products as cycles increase, resulting in the increase of interface resistance.

Performing free discharge tests at different current density, namely limiting the discharge cut-off voltage in Na-O₂ batteries (Figure 4c) in the pure oxygen atmosphere can obtain the maximum discharge capacity and discharge plateau. The result shows that the MBV-7 deliveries a higher discharge capacity (6350 mAh g^{-1} vs. 5750 mAh g^{-1} for its counterpart at 100 mA g^{-1} ; 5400 mAh g^{-1} vs. 4850 mAh g^{-1} its counterpart at 200 mA g^{-1} ; 4170 mAh g^{-1} vs. 3200 mAh g^{-1} for its counterpart at 300 mA g^{-1}) at the same current density, demonstrating the MBV-7 a higher capacity at the same current density. This improved performance of the MBV-7 is possibly attributed to its higher specific surface area, stronger light absorption ability, and lower photoelectron hole recombination ratio. Figure 4d shows the discharge/charge voltage difference of Na-O₂ batteries with MBV-0 and MBV-7 as cathode catalysts at different current densities. The voltage difference is calculated based on the peak voltage of discharge/charge curves (Figure S5) to represent the polarization degree of the batteries. Obviously, at the same current density, the polarization degree of MBV-7 is smaller than that of MBV-0. At a current density of 100 mA g^{-1} , the discharge/charge voltage difference of MBV-7 is only about 1.07 V . When the current density increases to 200 mA g^{-1} , the discharge/charge voltage difference of MBV-7 is 1.16 V . Even if the current density continues to increase to

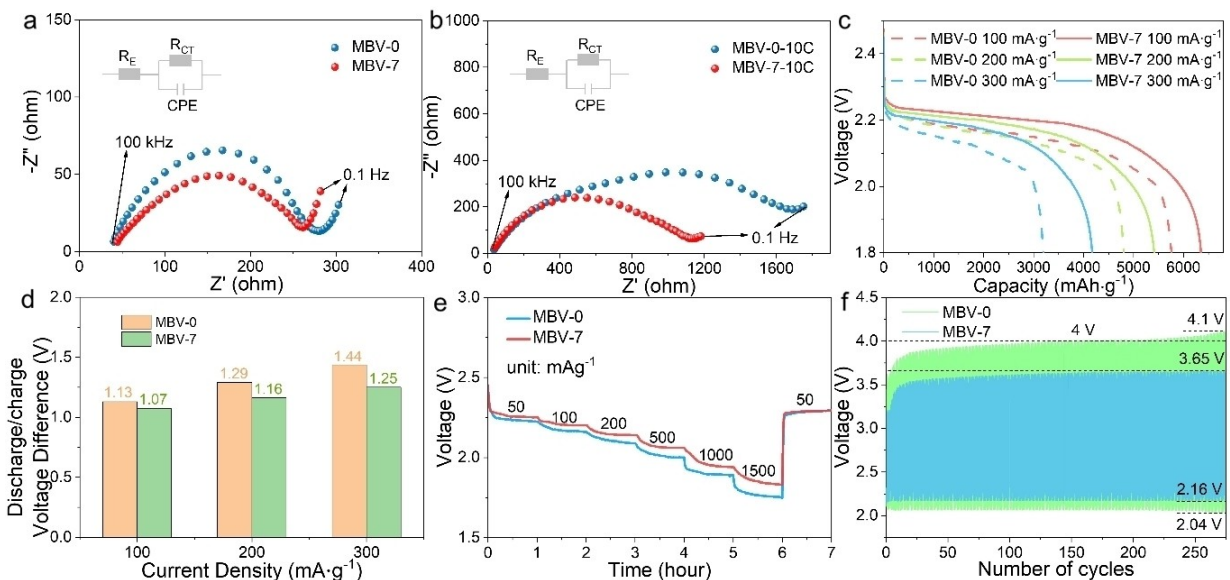


Figure 4. EIS for the a) 0, and b) 10 cycles discharge-charge testing in Na-O₂ batteries; c) the free-discharge curves, d) the discharge-charge voltage difference at different current densities; e) the rate capability, and f) the long cycling performance of MBV-0 and MBV-7 in Na-O₂ batteries.

300 mAg⁻¹, the discharge/charge voltage difference is only 1.25 V, lower than that of MBV-0 (1.44 V). The decrease in polarization represents the high catalytic activity of the MBV-7 catalyst.

The rate capability of the Na–O₂ battery is shown in Figure 4e. It is well known that as the discharge current density increases, the demand for oxygen molecules, electrons and ions during discharge process of the battery increases. Because of the mass transfer limitations, the supply of oxygen and ions is insufficient, resulting in a continuous decrease in rate performance. It is worth noting that under the same discharge current density conditions, the discharge voltage of MBV-7 is always higher than MBV-0. Even at a current density of 1500 mAg⁻¹, the discharge potential of MBV-7 remains above 1.8 V. This indicated the MBV-7 the better photocatalytic performance and faster electron transfer ability than the MBV-0. Figure 4f shows the cycling performance of the Na–O₂ battery using MBV-0 and MBV-7 as catalysts evaluated by the constant current method. With a current density of 200 mAg⁻¹, the discharge potential of MBV-7 is above 2.16 V for over 270 cycles. However, under the same conditions, the discharge potential of MBV-0 is significantly lower (2.1 V) and finally reduced to 2.04 V, indicating an increase in its discharge polarization. During the charging process, the potential of MBV-7 slightly increases, then gradually stabilizes at 3.65 V and the battery operates stably for over 270 cycles (Figure S6). In contrast, MBV-0 operates stably below a charging potential of 4 V for 150 cycles, and then its voltage increases to the final 4.1 V. It is well known that a huge overpotential during charging will threaten the stability of the battery and reduce the energy efficiency of the battery.^[7] Compared with the ever-reported solid catalysts (Table S3), MBV-7 significantly reduces the overpotential, which is beneficial for long cycle life of Na–O₂ batteries. For elucidating the importance of the illumination on the MBV-7 photocatalyst, we tested the discharge-charge curves of Na–O₂ batteries under no illumination (Figure S7). It showed an over 4 V initial charge potential compared with the illumination (<3.55 V) and a fast-increasing charge potential. Under the illumination, the charge potential is stable, indicating the lasting-stable catalytic activity of the MBV-7 and the huge role of the MBV-7 under illumination.

To further analyze the reaction features of Na–O₂ batteries, the discharge products on the MBV-7 and MBV-0 cathodes were observed using a scanning electron microscope (SEM). For comparison, the undischarged in-situ positive electrode is shown in Figure S8. As shown in Figure 5a and b, the discharge products of MBV-7 are essentially composed of many aggregated small particles with sizes below 300 nm. In contrast, the discharge product particles of MBV-0 are larger and significantly fewer. It was reported that the smaller size discharge products are easier to decompose, which means the MBV-7 a better capability to decompose discharge products than its counterpart.^[31] Meanwhile, more discharge products indicate that MBV-7 has a higher discharge efficiency, demonstrating its superior ORR reaction kinetics.

The XRD patterns for the discharged MBV-7/CNTs cathode operated in Na–O₂ batteries show a characteristic diffraction

peak corresponding to Na₂O₂ at 26° (Figure 5c), indicating Na₂O₂ as the main discharge products. This reveals that the addition of BiVO₄ photocatalyst wouldn't alter the oxygen reduction reaction mechanism for the aprotic Na–O₂ battery. After charging, the signal peaks attributed to Na₂O₂ disappeared, indicating the decomposition of the formed Na₂O₂. Further analysis of the composition of the discharge products using Raman (Figure 5d) shows that the discharge products on MBV-0 and MBV-7 are the mixture of NaO₂ and Na₂O₂, consistent with previous reported studies, where NaO₂ was first generated through electrochemical reaction and subsequently converted into Na₂O₂ through chemical conversion.^[14,32] The much stronger NaO₂ signal on the Raman spectra manifested more NaO₂ formation, which was possibly contributed to the much faster and more one-electron reactions on the MBV-7 catalysts due to its faster reaction kinetics as well as the much more reaction sites as the above Tafel, CV and BET proved. As for the absent signal for NaO₂ in the discharged MBV-7/CNTs electrode, it may be due to the poor crystallinity for the formation of the nanosized NaO₂. Meanwhile, the charged cathode XRD result is consistent with the pristine undischarged result, indicating the stability of BiVO₄.

For further unveiling the improved performance of photoelectrocatalysis, the first principles calculation was employed to explore the electronic structure. As shown in Figure 6a and b, the band gap calculated of BiVO₄ is 1.86 eV, and the band gap of Mo-doped BiVO₄ slightly decreases (1.81 eV), which is conducive to light energy absorption. Moreover, there are significant changes in the energy levels at the valence band edge and conduction band edge, indicating that the position of the band edge has changed due to Mo doping. A small gap state below the Fermi level, mainly from the Mo 4d state was detected, which is beneficial for charge transfer. What's more, it shows a lower work function obtained in Mo-dope BiVO₄ than pure BiVO₄, representing the easier electron extraction, namely the fine light excitation and conductivity for the doped one (Figure 6c and S9). It is well known that the whole charging polarization of Na–O₂ batteries is determined by Na₂O₂ decomposition as the following successive steps:^[33]



According to the calculation of adsorption energy, the adsorption energy of Mo-doped BiVO₄ for Na₂O₂ (-4.157 eV) and NaO₂ (-1.842 eV) are both significantly stronger than that of undoped BiVO₄ (Figure 6d), indicating the easier decomposition capability.

As a potential energy storage device in future, Na–O₂ battery with the Mo-doped BiVO₄ catalysts is also run in natural sunlight. As shown in Figure S10, the discharge/charge potential under natural sunlight is between the dark and simulated sunlight. The increased charge potential under natural sunlight is possibly due to the low intensity of light. In our region, the total solar radiation in a year is around

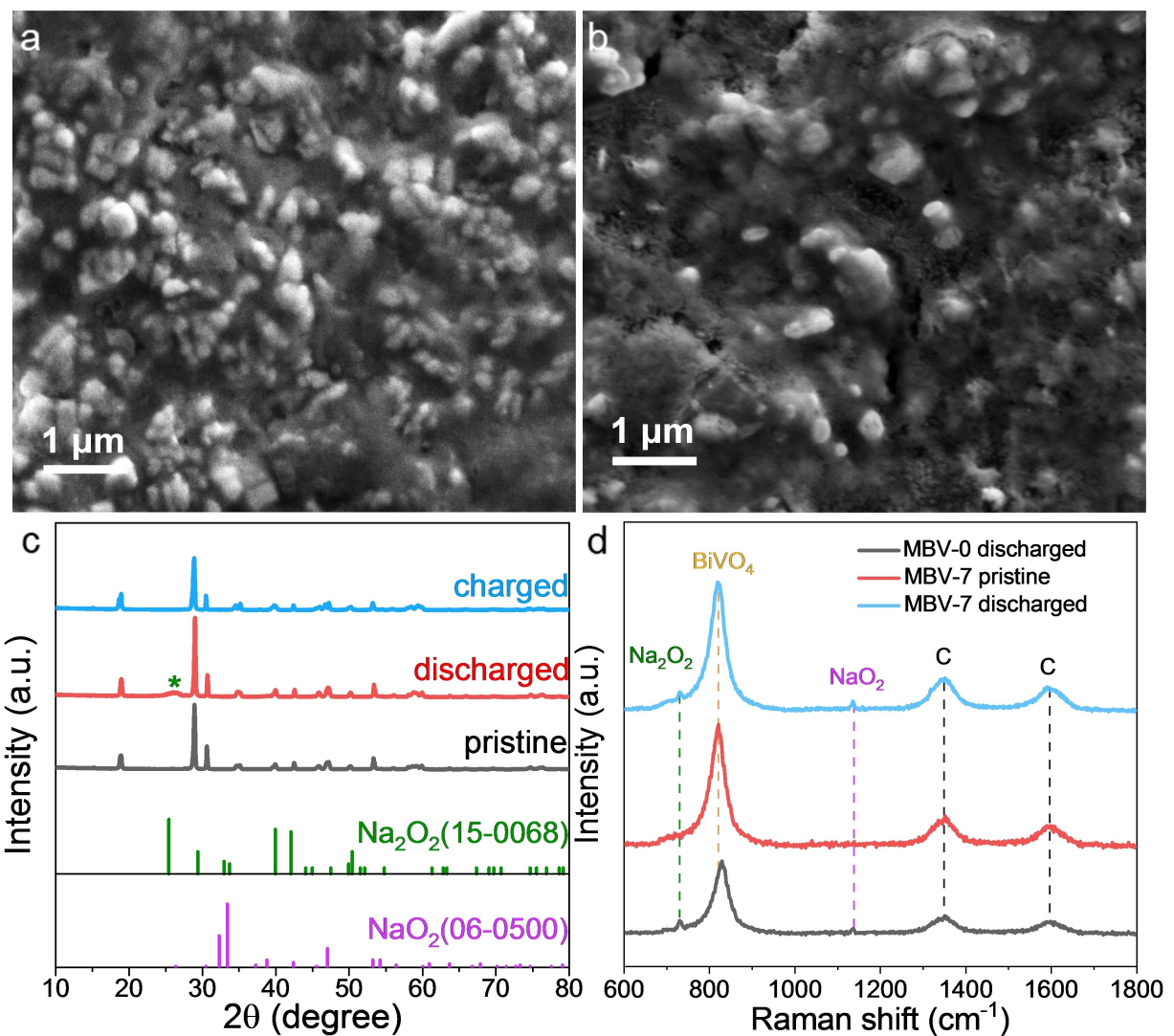


Figure 5. SEM images of the discharged a) MBV-7 cathode, and b) MBV-0 cathode; c) XRD spectra of the MBV-7/CNTs cathode operated in $\text{Na}-\text{O}_2$ batteries; d) Raman spectra of the MBV-7/CNTs and MBV-0/CNTs cathode operated in $\text{Na}-\text{O}_2$ batteries.

1200 kWh m⁻² (Figure S11), while the annual sunshine time is 1000–1400 h (data from CEIC), resulting in an average solar radiation intensity of 0.85–0.12 W cm⁻², which is approximately equivalent to 1 sun. However, the solar irradiation is lower in winter as well as the blockage of light due to the thick clouds, so the solar radiation intensity in our region during winter is lower than the simulated sunlight irradiation (0.1 W cm⁻²). The lower the light intensity, the less excitation of BiVO_4 , and thus results in low photocurrent density for slow electrode reactions with increased polarization. Therefore, for the future application of the light-assisted $\text{Na}-\text{O}_2$ batteries after solving the stability of Na metal anode and organic electrolyte, they can be operated on the region with rich solar irradiation, such as the Sahara desert.

3. Conclusions

In conclusion, the Mo-doped BiVO_4 on the influence of the performance of $\text{Na}-\text{O}_2$ batteries was studied. A certain Mo doping reduces not only the size of BiVO_4 , but also the recombination of photogenerated carriers. These greatly improve the light absorption intensity as well separation efficiency of charge carrier compared with its counterpart. Further electrochemical performance in $\text{Na}-\text{O}_2$ batteries shows Mo-doped BiVO_4 reduces the electron transfer resistance, boosts ORR and OER reaction kinetics, thus improving its rate performance. The calculation shows the Mo-doped BiVO_4 an easier electron extraction for fine light excitation as well as stronger interaction with Na_2O_2 for charging. This study displays positive relation of the light absorption intensity as well as separation efficiency of charge carrier in photocatalysts with the performance of $\text{Na}-\text{O}_2$ batteries and provides a guide to speed up the development of aprotic aqueous alkali metal-oxygen batteries.

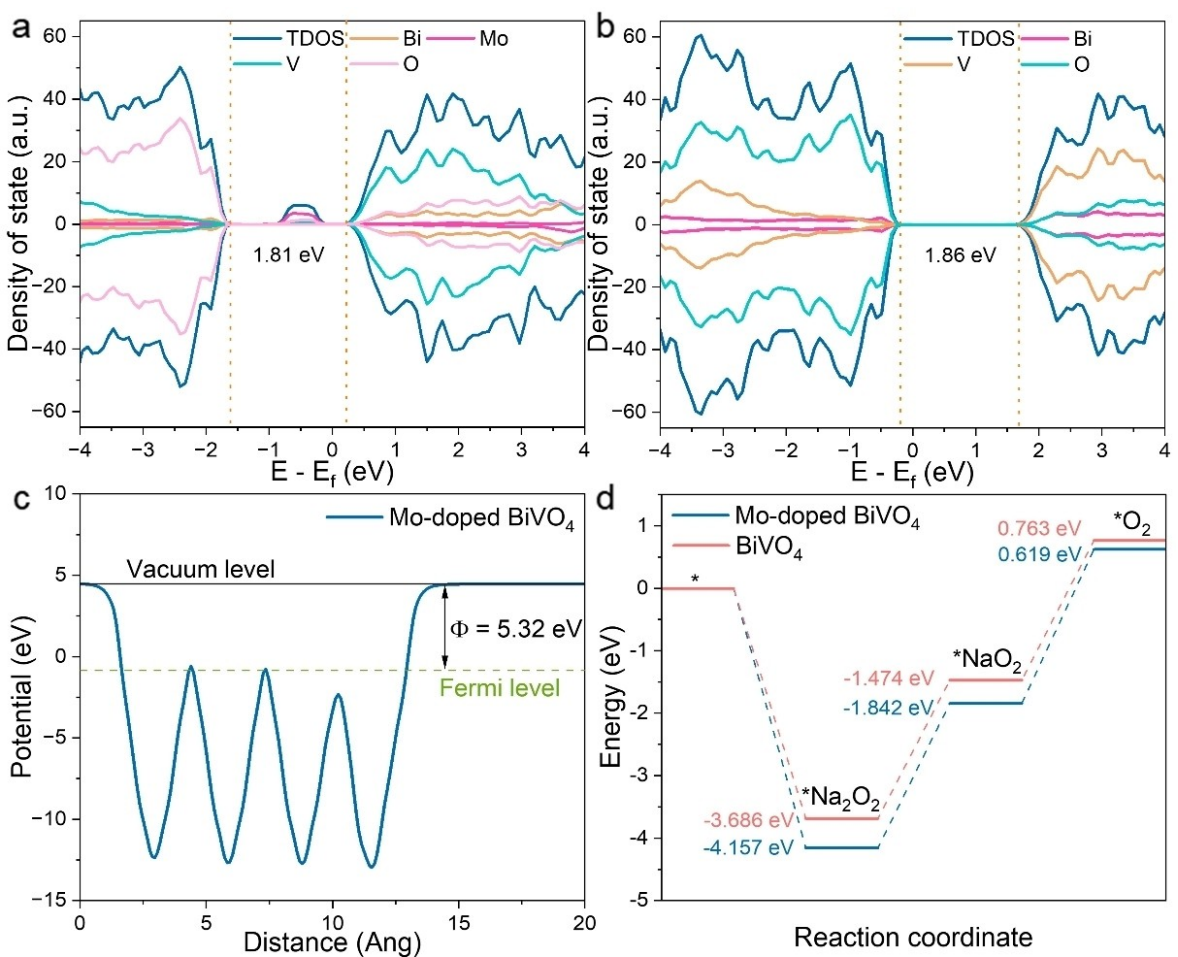


Figure 6. The density of states for a) Mo-doped BiVO_4 , and b) BiVO_4 ; c) The work function for the Mo-doped BiVO_4 , d) the adsorption energy profile for the Na_2O_2 decomposition with the assistance of pure BiVO_4 and Mo-doped BiVO_4 (the * represents the base material BiVO_4 or Mo-doped BiVO_4).

Experimental Section/Methods

Preparation of Pure BiVO_4 : Firstly, dissolving 5 mmol of $\text{Bi}(\text{NO}_3)_3 \cdot 5\text{H}_2\text{O}$ in 20 ml of 4 mol/L HNO_3 solution and stirring thoroughly for one hour was to obtain clear solution A; dissolving 5 mmol of NH_4VO_3 in 20 mL of 4 mol/L sodium hydroxide solution and stirring thoroughly for one hour was to obtain clear solution B. Secondly, mixing solutions A and B and stirring thoroughly for one hour was to obtain orange yellow solution C. The pH of solution C was adjusted to 6 using $\text{NH}_3 \cdot \text{H}_2\text{O}$ and CH_3COOH . Afterwards, the solution C was transferred to a Teflon-lined stainless-steel autoclave and heated at 160 °C for 12 hours. After the autoclave was naturally cooled to room temperature, a series of operations such as filtration, washing, and centrifugation were carried out to obtain a bright yellow precipitate, which was then dried in a 60 °C oven for 12 hours to obtain pure BiVO_4 .

Preparation of Mo-Doped BiVO_4 : similar to the preparation process of pure BiVO_4 , the rest of the preparation is consistent except for solution B. During the preparation process, solution B replaces NH_4VO_3 with a certain amount of $(\text{NH}_4)_2\text{MoO}_4$, which corresponds to V with an equal number of Mo atoms. The proportion of doped Mo was used as the doping rate of the material.

Preparation of Electrodes: Firstly, 0.6 g of polyvinylidene fluoride was dissolved in 10 mL of NMP and stirred thoroughly for 12 hours to obtain the viscous solution D. Next, 0.08 g BiVO_4 and 0.02 g carbon nanotubes evenly were mixed and added them to

the grinder, then 0.3 mL of solution D was added and grinded thoroughly for 10 minutes to form the stable mixture. Finally, the mixture was casted evenly on carbon paper and dried in a 60 °C oven for 12 hours. Finally, the dried carbon paper is stamped into a BiVO_4 cathode with a diameter of 12 mm and a loading capacity of 0.6 mg.

Assembly of $\text{Na}-\text{O}_2$ Batteries: 1.72 g NaCF_3SO_3 was dissolved in a glove box filled with argon and stirred thoroughly in 20 mL tetraethylene glycol dimethyl ether (TEGDME) for 12 hours to obtain a 0.5 M $\text{NaCF}_3\text{SO}_3/\text{TEGDME}$ electrolyte. All $\text{Na}-\text{O}_2$ batteries were assembled in a glove box with a 2025-type coin battery. As shown in Figure S12a, $\text{Na}-\text{O}_2$ battery is obtained by successively combining the 12 mm diameter sodium metal round foil cut from Na block as anode, glass fiber separator, 80 μL electrolyte, 20 μL electrolyte, BiVO_4 cathode and foam nickel as support material. In order to optimize the battery testing environment, it is necessary to load the battery into a testing container for three alternating vacuuming and charging with pure O_2 . Then the battery test container was sealed and stood for 3 hours for electrochemical testing.

Characterization: The Powder X-ray diffraction (XRD) measurement of BiVO_4 and cathode were conducted on PANalytical X'Pert Powder with Cu $\text{K}\alpha$ radiation (Spectris Pte. Ltd, The Netherlands). The morphology of BiVO_4 and discharge products were analyzed by scanning electron microscope (SEM, JEOL JSM-6700, Japan). The

structure of BiVO_4 was gained on a FEI Tecnai G2 F30 transmission electron microscope (TEM, Thermo Fisher Scientific CDLtd, Czech Republic) with the sample deposited on a copper grid. Raman spectra were obtained at a laser wavelength of 532 nm by the Horiba LabRAM HR evolution microscope (HORIBA Jobin Yvon S.A.S. France). Approximately 8% of the maximum laser power (13 mW) was used for preventing laser from damaging the CNTs. X-ray photoelectron spectroscopy (XPS) of BiVO_4 was tested on an ESCALAB 250Xi (Thermo Fisher Scientific, USA). The UV-Vis diffuse reflectance spectra were collected on a UV-2550PC spectrophotometer (Shimadzu, Japan), using BaSO_4 as the reference with a wavelength range of 200–800 nm. Nitrogen adsorption-desorption isotherms for measuring specific surface area were obtained on a multistation surface and porosity analyzer max-II (MicrotracBEL, Japan).

Electrochemical and Photoelectrochemical Measurements of $\text{Na}-\text{O}_2$ Batteries: Electrochemical impedance spectroscopy (EIS), cyclic voltammetry (CV) and linear sweep voltammetry (LSV) measurements for $\text{Na}-\text{O}_2$ batteries were performed on the Biologic SP-200 electrochemical workstation. The EIS frequency range is 10^5 – 10^{-1} Hz. For CV and LSV testing, a dual electrode setup is used, where the sodium anode is not only used as a counter but also as a reference electrode, and the $\text{BiVO}_4/\text{CNTs}$ cathode is used as the working electrode. On the LAND CT3001 A multi-channel battery tester, a constant current discharge/charge test was performed in the $\text{Na}-\text{O}_2$ batteries within the voltage range of 1.8 to 4.1 V. $\text{Na}-\text{O}_2$ batteries were discharged to 1.8 V to obtain the maximum discharge capacity of the battery in a pure oxygen atmosphere. The cyclic test is controlled by limiting capacity at a constant current density. As shown in Figure S12b, a 300 W Xe light source is used to provide illumination for the electrochemical performance testing of $\text{Na}-\text{O}_2$ batteries.

Computational Methods: All calculations were used by the Vienna ab initio Simulation Package (VASP).^[34,35] The generalized gradient approximation (GGA) using the Perdew-Burke-Ernzerhof (PBE) formulation and the projected augmented wave (PAW) potentials we chosen to describe the ionic cores and take valence electrons into account using a plane wave basis set with a kinetic energy cutoff of 450 eV.^[36,37] Partial occupancies of the Kohn-Sham orbitals were allowed using the Gaussian smearing method and a width of 0.1 eV. The electronic energy was considered self-consistent when the energy change was smaller than 10^{-5} eV. A geometry optimization was considered convergent when the energy change was smaller than -0.02 eV/Å. A single gamma-point k-point grid for Brillouin zone was used for geometry optimization and $2\times 2\times 1$ k-point for electrostructure calculation. DFT+U was used for this calculation, which U=3 eV and 2.7 eV for V and Mo, respectively.

Supporting Information

Supporting Information is available from the Wiley Online Library or from the author.

Acknowledgements

The authors are grateful for the support received from the National Natural Science Foundation of China (NSFC, Grant No. 22005041), the State Key Laboratory of Mechanical Transmissions Project (SKLMT-ZZKT-2017 M11), the Fundamental Research Funds for the Central Universities (2022CDJXY-007),

the 111 Project of the Ministry of Education, China (No. B08036).

Conflict of Interests

The authors declare no conflict of interest.

Data Availability Statement

Research data are not shared.

Keywords: $\text{Na}-\text{O}_2$ batteries · BiVO_4 · Molybdenum doping · reaction kinetics · polarization · fast electron transfer

- [1] Q. Sun, L. Dai, Y.-F. Tang, J. Sun, W.-D. Meng, T.-T. Luo, L. Wang, S. Liu, *Small Methods*. **2022**, *6*, 2200345.
- [2] M. V. Reddy, A. Mauger, C. M. Julien, A. Paoletta, K. Zaghib, *Materials*. **2020**, *13*, 1884.
- [3] C. Yu, S. Ganapathy, E. R. H. v. Eck, H. Wang, S. Basak, Z. Li, M. Wagemaker, *Nat. Commun.* **2017**, *8*, 1086.
- [4] H.-M. Sun, J. Lv, Z.-P. Sun, C.-J. Ding, W.-W. Huang, *J. Mater. Chem. A*. **2022**, *10*, 6096.
- [5] Y.-F. Tang, T.-T. Yang, J.-Z. Chen, H. Li, H.-J. Ye, C.-C. Du, Y.-S. Tang, M.-R. Xia, T.-D. Shen, L.-Q. Zhang, J.-Y. Huang, *J. Mater. Chem. A*. **2022**, *10*, 20294.
- [6] L. Geng, L.-L. Li, H. Zhang, M.-J. Zhong, P. Mu, J. Li, *J. Mater. Chem. A*. **2022**, *10*, 14875.
- [7] N. E. Bentj, G. S. Gurmesa, C. A. Geffe, A. M. Mohammed, G. A. Tiruye, Y. S. Mekonnen, *J. Mater. Chem. A*. **2022**, *10*, 8501.
- [8] Y. Kang, S. Wang, S. Zhu, H. Gao, K. S. Hui, C.-Z. Yuan, H. Yin, F. Bin, X.-L. Wu, W. Mai, *Appl. Catal. B*. **2021**, *285*, 119786.
- [9] J. Ma, Y. Li, N. S. Grundish, J. B. Goodenough, Y. Chen, L. Guo, Z. Peng, X. Qi, F. Yang, L. Qie, *J. Phys. D* **2021**, *54*, 183001.
- [10] Y. Liu, X. Chi, Q. Han, Y. Du, J. Yang, Y. Liu, *J. Alloys Compd.* **2019**, *772*, 693.
- [11] Y. S. Jeong, J.-B. Park, H.-G. Jung, J. Kim, X. Luo, J. Lu, L. Curtiss, K. Amine, Y.-K. Sun, *Nano Lett.* **2015**, *15*, 4261.
- [12] Y. Yao, F. Wu, *ACS Appl. Mater. Interfaces*. **2017**, *9*, 31907.
- [13] X. Yang, C. Peng, M. Hou, D. Zhang, B. Yang, D. Xue, Y. Lei, F. Liang, *Adv. Funct. Mater.* **2022**, *32*, 2201258.
- [14] S. Kang, Y. Mo, S. P. Ong, G. Ceder, *Nano Lett.* **2014**, *14*, 1016.
- [15] Q.-Y. Shen, J.-L. Ma, M.-L. Li, W. He, Y.-Y. Tan, P.-Y. Zhou, Y. Wang, *Batteries*. **2022**, *8*, 227.
- [16] M. Sun, Z. Zhang, Q. Shi, J. Yang, M. Xie, W. Han, *Chin. Chem. Lett.* **2021**, *32*, 2419.
- [17] M. Zhou, J. Bao, Y. Xu, J. Zhang, J. Xie, M. Guan, C. Wang, L. Wen, Y. Lei, Y. Xie, *ACS Nano*. **2014**, *8*, 7088.
- [18] P. Subramanyam, T. Vinodkumar, D. Nepak, M. Deepa, C. Subrahmanyam, *Catal. Today*. **2019**, *325*, 73.
- [19] A. Polo, M. V. Dozzi, I. Grigioni, C. Lhermitte, N. Plainpan, L. Moretti, G. Cerullo, K. Sivula, E. Sellia, *Solar RRL*. **2022**, *6*, 2200349.
- [20] B. Liu, X. Yan, H. Yan, Y. Yao, Y. Cai, J. Wei, S. Chen, X. Xu, L. Li, *Materials*. **2017**, *10*, 976.
- [21] A. Iwase, S. Nozawa, S.-I. Adachi, A. Kudo, *J. Photochem. Photobiol. A*. **2018**, *353*, 284.
- [22] M. C. Abello, M. F. Gomez, L. E. Cadus, *Catal. Lett.* **1998**, *53*, 185.
- [23] M. Zhang, C. Shao, X. Li, P. Zhang, Y. Sun, C. Su, X. Zhang, J. Ren, Y. Liu, *Nanoscale*. **2012**, *4*, 7501.
- [24] S.-M. Lee, S.-N. Cho, J. Cheon, *Adv. Mater.* **2003**, *15*, 441.
- [25] W. Li, Y. Zhang, Y. Bu, Z. Chen, *J. Alloys Compd.* **2016**, *680*, 677.
- [26] R. Wang, L. Cao, *J. Alloys Compd.* **2017**, *722*, 445.
- [27] R. L. Frost, D. A. Henry, M. L. Weier, W. Martens, *J. Raman Spectrosc.* **2006**, *37*, 722.
- [28] D. Zhou, W. G. Qu, C. A. Randall, L. X. Pang, H. Wang, X. G. Wu, J. Guo, G. Q. Zhang, L. Shui, Q. P. Wang, *Acta Mater.* **2011**, *59*, 1502.
- [29] S. Mehraj, M. S. Ansari, Alimuddin, *Thin Solid Films*. **2015**, *589*, 57.

- [30] D. Schröder, C. L. Bender, R. Pinedo, W. Bartuli, M. G. Schwab, Ž. Tomović, J. Janek, *Energy Technol.* **2017**, *5*, 1242.
- [31] J. Fu, X. Guo, H. Huo, Y. Chen, T. Zhang, *ACS Appl. Mater. Interfaces.* **2019**, *11*, 14803.
- [32] S. Yang, D. J. Siegel, *Chem. Mater.* **2015**, *27*, 3852.
- [33] B. Xu, D. Zhang, C. Peng, F. Liang, H. Zhao, B. Yang, D. Xue, Y. Lei, *Adv. Energy Mater.* **2023**, *13*, 2302325.
- [34] M. Yu, Y. Tang, Y. Liao, W. He, X.-X. Lu, X. Li, *J. Mater. Sci. Technol.* **2023**, *165*, 225.
- [35] G. Kresse, J. Furthmüller, *Comput. Mater. Sci.* **1996**, *6*, 15.
- [36] J. P. Perdew, K. Burke, M. Ernzerhof, *Phys. Rev. Lett.* **1996**, *77*, 3865.
- [37] P. E. Blöchl, *Phys. Rev. B.* **1994**, *50*, 17953.

Manuscript received: January 30, 2024

Revised manuscript received: February 27, 2024

Accepted manuscript online: March 2, 2024

Version of record online: March 15, 2024